Appl Phys A (2011) 103: 33–42
DOI 10.1007/s00339-011-6304-5

Applied Physics A
Materials Science & Processing

Burstein–Moss shift and room temperature near-band-edge luminescence in lithium-doped zinc oxide

N. Rajeswari Yogamalar · A. Chandra Bose

Received: 24 September 2010 / Accepted: 17 January 2011 / Published online: 9 February 2011

Abstract Nanopowders of pure and lithium-doped semiconducting ZnO ($Zn_{1-x}Li_xO$, where $x = 0, 0.01, 0.03, 0.06, 0.09$ and 0.15 in atomic percent (at.%)) are prepared by PEG-assisted low-temperature hydrothermal method. The average crystallite size is calculated using Debye–Scherrer formula and corrected for strain-induced broadening by Williamson–Hall (W–H) plot. The peak shift in XRD and the lattice constant of ZnO as a function of unit cell composition are predicted by Vegard's law. The evolution of ZnO nanostructures from rod-shaped to particle nature is observed from TEM images and the influence of dopant on the morphology is investigated. The optical absorption measurement marks an indication that the incorporation of lithium ion into the lattice of ZnO widens the optical band gap energy from ∼2.60 to ∼3.20 eV. The near band edge (NBE) emission peak centered at ∼3.10 eV is considered to be the dominant emission peak in the PL spectra. Blue emission peak is not observed in doped ZnO, thus promoting defect-free nanoparticles. The Burstein–Moss shift serves as a qualitative tool to analyze the widening of the optical band gap and to study the shape of the NBE luminescence in doped ZnO nanopowders. FT-IR spectra are used to identify the strong metal–oxide (Zn–O) interaction.

1 Introduction

Wurtzite structure nanosized ZnO has been identified as one of the most important metal oxides in view of its numerous applications. It is a promising n-type semiconducting material with wide band gap of 3.37 eV, large exciton binding energy of 60 meV, promoting it to have an extensive applications in gas sensing, catalysis, energy storage, optoelectronic devices, UV lasing action, surface acoustic wave devices, piezoelectric transducers, blue light emitting diodes, transparent conducting oxides, and many more [1–6]. In addition, it is highly expected to explore the novelties in electronic and optical devices, notably in lasers, where the wavelength of the light can be tuned more precisely [7]. The growth, properties and applications of nanosized ZnO are systematically reviewed and reported by Wang, Ozgur et al., Schmidt-Mende and MacManus-Driscoll, and Baruah and Dutta [8–11].

The electronic band structure and its optimization are of great importance in designing semiconductor devices and it can be simulated by changing the material crystal structure and chemical composition. As the impurity atoms are introduced, the spatial geometries which are providing the lowest energy configuration in the bulk may not provide the same as when the surface atoms and surface bonds are altered. Such modifications are much important in many electronic and optoelectronic devices, especially illustrated in injection lasers and bipolar transistors [12]. Theoretically and experimentally, the importance of dopants and their influence on optical and transport properties are evaluated [13]. To achieve stable p-type ZnO, dopants from I and V group elements are introduced and their property studies including structure, morphology, optical, magnetic and transport properties are updated periodically [14–16]. Few citations refer that the addition of lithium tremendously increases the electrical resistivity and hence is applied to transparent conducting oxides (TCO) electrodes, piezoelectric devices and memory devices [17–19]. As the diffusion capability is greater, the lithium-doped ZnO act as effective catalysts

N.R. Yogamalar · A. Chandra Bose (✉)
Nanomaterials Laboratory, Department of Physics,
National Institute of Technology, Tiruchirappalli 620 015, India
e-mail: acbose@nitt.edu
Fax: +91-431-2500133

for the trans-esterification of soya-bean oil with methanol [20]. A stable *p*-type lithium-doped ZnO nanopowders, utilized for dye sensitized solar cell exhibiting an efficiency of ∼53%, are synthesized by conventional method [21, 22]. In our experimental work, a facile chemical precipitation method is approached to synthesize lithium-doped ZnO and their material characteristics are well described. The details reporting the synthesis of lithium-doped ZnO with reduced crystallite size are consistently compared with the published data.

The current studies are mainly concentrated on optical absorption, Burstein–Moss shift caused by heavy hole concentration and NBE emission shift in doped ZnO. The optical band gap of a semiconductor is the minimum energy required to move an electron from its bound energy state (valence band) to a free energy state (conduction band) where it can participate in conduction. Apart from doping, several other factors are believed to affect the electronic transition in the metal–oxide nanostructures. They are excitonic transitions (exciton-related recombinations), alloy-induced structural disorders or lattice distortion effects, quantum confinement or quantum surface effects, presence of surface defects such as oxygen vacancies and interstitials [23, 24]. Wang et al. discussed the size-dependent electronic band structure of ZnO nanowires [25]. The above effects can construct either a narrowing or widening of the optical band gap at higher carrier concentration due to randomly distributed impurities and shift in Fermi energy. The Burstein–Moss effect and Quantum size confinement effect (QSE) are the two well-known phenomena explaining the widening of the band gap in heavily doped semiconductors [26, 27]. The indirect band gap transition, band–band transition, impurity band formation, band–shallow acceptor transition are few other factors influencing the band gap widening in semiconductor metal–oxide nanoparticles [28, 29]. As the particle size confines to a nanoscale regime, the band structure of semiconductor changes. According to QSE, the ionic core level in the crystal compound shifts and the band gap width revises concurrently, as the quantum and surface effects become more significant. In *p*-type semiconducting material, the widening of the band gap shifts the absorption edge towards the higher energy level as they create vacancy in the valence band. They further drag the acceptor energy level inward resulting in broadening of band gap. As an outcome, in heavily doped semiconductor the electronic transition originates from the Fermi level in valence band to the conduction band. This shift in absorption edge or Fermi energy level due to heavy doping is referred to as Burstein–Moss shift and is reported in ZnMgO nanowires with different doping concentrations [30]. Similarly, the blue shift in NBE luminescence explained on the basis of Burstein–Moss shift is pointed out by Makino et al. in *n*-type Ga-doped ZnO [31].

This paper addresses the synthesis of lithium-doped ZnO by polyethylene glycol (PEG) assisted low-temperature hydrothermal method and the composition of lithium ranges from 0 to 15 at.%. The enhancement of optical band gap due to insertion of lithium ions has been interpreted in terms of contraction of lattice distortion or dislocation, morphology evolution and partial removal of the available electronic states in the valence band, so that the topmost electronic states are vacant. The above consequences result in widening of band gap in lithium-doped ZnO. An experimental study of the dopant-dependent band gap shift and line broadening of the excitonic luminescence in ZnO, derived from the optical absorption and PL measurements, are outlined. The Burstein–Moss effect and size-related confinement are responsible for the band gap widening in lithium-doped ZnO.

2 Experimental

2.1 Materials and method

Hydrothermal method is a simple and cost-effective method where the kinetics of the chemical reaction can be accelerated tremendously. Pure ZnO with the mean diameter of ∼42 nm is obtained through long chain surfactant molecule PEG-directed hydrothermal method with zinc chloride as a starting precursor. The ZnO nanopowders are doped by the addition of lithium chloride to the starting solution. Zinc chloride, $ZnCl_2$ (Qualigens India 98%), lithium chloride, LiCl (Loba Chemicals), ammonia and PEG are purchased from Merck Chemical Company and are used without purification. Throughout the synthesis the double distilled water is used for aqueous solution preparation.

Here, a solution mixture of zinc chloride and lithium chloride in appropriate atomic ratio is used to synthesize pure and lithium-doped ZnO. A surfactant solution of 0.1 mM PEG (Mol. wt. 40,000) is prepared and added to the dissolved solution of zinc chloride and lithium chloride precursors. After stirring for 60 min, ammonia solution is added drop-wise until the pH value of the solution reaches 7–8. The white precipitate obtained is allowed to settle and 80 ml of the solution mixture is poured into Teflon lined stainless steel autoclave of 100 ml capacity and heated at 160°C for 20 h in order to incorporate the dopant ion. The resulting white precipitate is centrifuged with ethanol and distilled water repeatedly. Finally, the precipitate is dried at room temperature and collected for various characterizations. The influence of dopant on the structure, morphology and optical properties of ZnO is recognized by varying the dopant concentration from 0 to 15 at.%. The as-synthesized $Zn_{1-x}Li_xO$ sample products are designated as LiX, where X is the dopant concentration numbered as 0, 1, 3, 6, 9 and 15 in at.%.

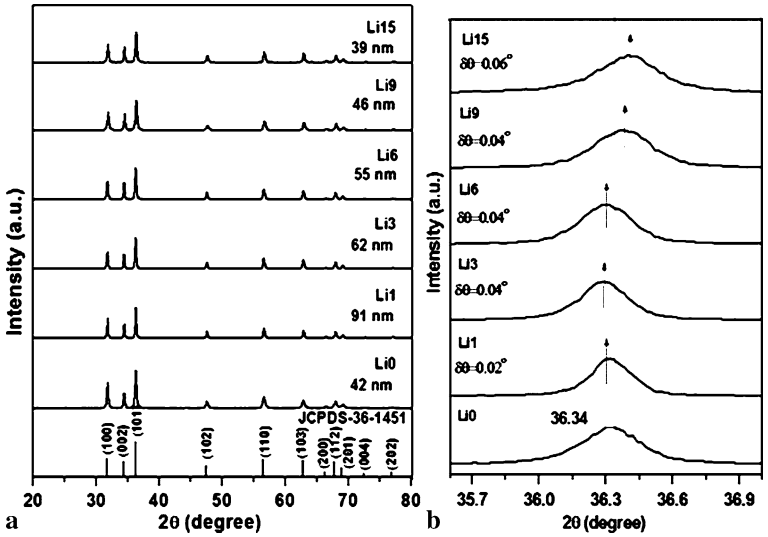

Fig. 1 (**a**) XRD powder diffraction pattern of $Zn_{1-x}Li_xO$ ($x = 0$, 1, 3, 6, 9, and 15 at.%) nanoparticles. (**b**) Changes in the (101) wurtzite peak position with lithium concentration

2.2 Characterization tools

The structure, morphology and crystallinity of lithium-doped ZnO are characterized by powder X-ray diffractometer (XRD), field emission scanning electron microscopy (FESEM), transmission electron microscopy (TEM) and selected area electron diffraction (SAED). XRD spectra are recorded using Ultima III Rigaku powder X-ray diffractometer, with Cu $K_{\alpha 1}$ source ($\lambda = 1.5406$ Å) in θ–2θ configuration. In X-ray analysis, the loose sample powder is leveled in the sample holder to ensure a smooth surface and mounted on a fixed horizontal sample plane. SEM images are obtained from Hitachi S4800 field emission scanning electron microscope. For TEM and electron diffraction analysis, Jeol JEM 2000 FX-II operating at 200 kV is used to examine the morphology of the undoped and 6 at.% of lithium-doped ZnO. Fourier transform infrared (FT-IR) spectrum of as-synthesized sample with standard KBr pellet is recorded using Perkin-Elmer FT-IR spectrometer in the range of 4000–400 cm^{-1}. In addition, the optical properties of lithium-doped ZnO samples with different dopant concentrations are also investigated. Room temperature optical spectra in the UV and visible light wavelength ranges are recorded using Shimadzu UV-1700 Pharma spectrophotometer. In the UV-vis absorption measurement, the spectrophotometer measures the absorbance of undoped and lithium-doped ZnO, relative to the standard sample powder of $BaSO_4$. The emission spectra are recorded using Shimadzu (RF-5301 PC) spectrofluorophotometer under an excitation wavelength of 230 nm using 150 W xenon lamp at room temperature.

3 Results and discussion

3.1 Phase confirmation

Figure 1a shows the XRD pattern of lithium-doped ZnO particles with different dopant concentrations. All the diffraction peaks are well indexed as pure hexagonal phase wurtzite structure, and even with an increase in dopant concentration from 0 to 15 at.%, the phase remains unaltered. The assignment of peak is made by comparing with the standard JCPDS data sheet (Card ID-36-1451). By doping with lithium, the dopant atoms occupy the Zn sites in ZnO lattice as their ionic radii are comparable. Thus, at room temperature they act as singly ionized acceptor with one extra hole. The average crystallite sizes of the entire as-synthesized lithium-doped sample are calculated using Debye–Scherrer approximation. The instrumental broadening are eliminated using the relation $\beta_{hkl} = (\beta_{meas} - \beta_{instr})$ where β_{hkl} is the instrumental corrected integral breadth of the reflection, in radians [32]. For this, the characteristic peak of ZnO (101) at $2\theta = 34.5°$ and their full width at half maximum (FWHM) are considered by using Cauchy Loretzian fit. The average crystallite size of Li0 is calculated to be 42 nm. As the doping concentration is increased from 1 to 15 at.%, there is a regular decrease in crystallite size from 91 to 40 nm indicating that the inclusion of dopant atom inhibits the growth of the particle. The lattice distortion and decrease in crystallite size are interpreted in terms of peak shift and peak width. At low carrier concentration, the XRD diffraction peak (101) has a FWHM of about 0.030 in radians, while at higher concentration, the FWHM increases to 0.045 radians. The broadening of the (101) peak can be attributed to the variation of density of free carriers and their presence produces crystal potential fluctuations. This random potential fluctuation due to redistribution, rearrangement of surface atoms

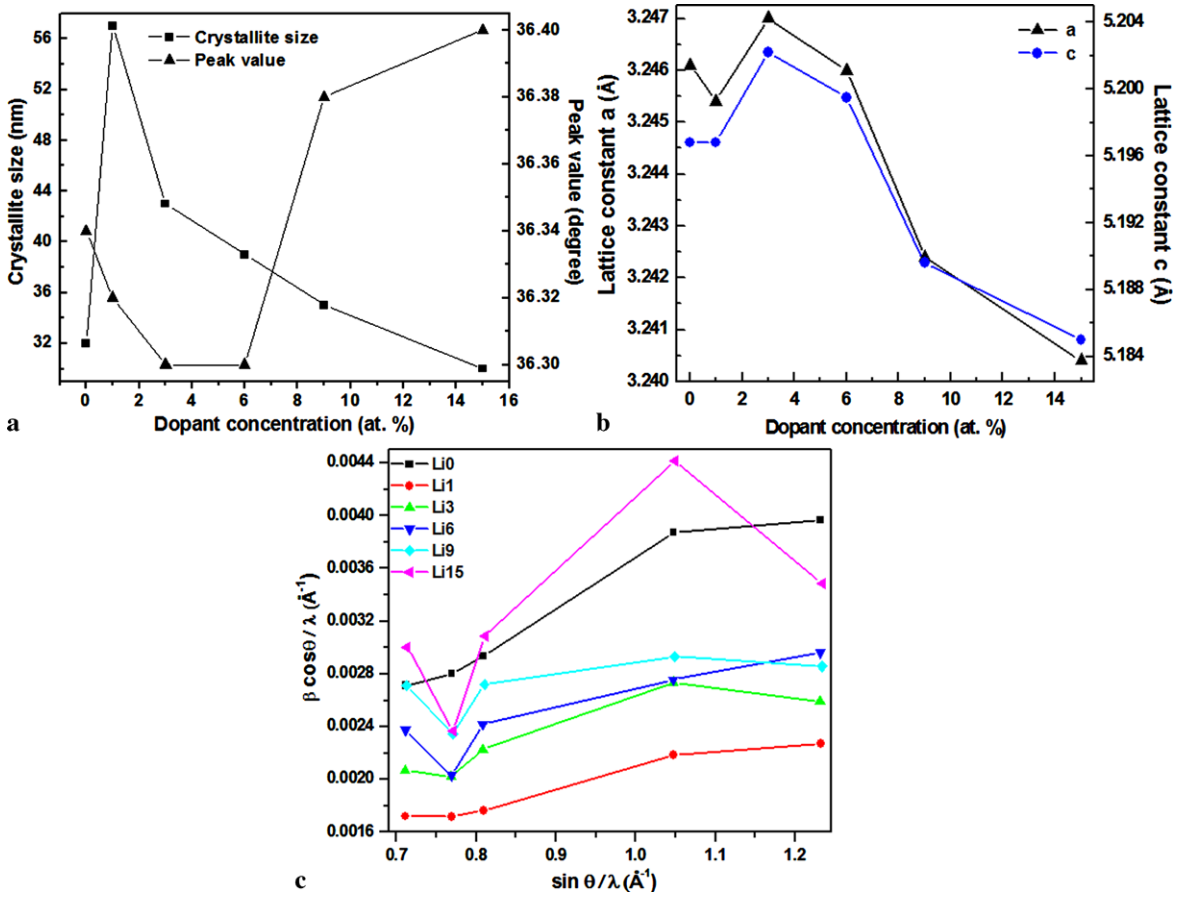

Fig. 2 (**a**) The shift in peak position $\delta\theta$ and the crystallite size variation. (**b**) Variation in the lattice parameters 'a' and 'c'. (**c**) W–H plot of wurtzite hexagonal phase ZnO as a function of dopant concentration

and alteration of surface bonding, shifts the peak position (101) accordingly. The shift in peak position and the calculated value of $\delta\theta$ are represented in Fig. 1b with respect to undoped ZnO. Compared with undoped ZnO, in lithium-doped ZnO at higher concentration the lithium atoms are highly confined and localized in the ZnO lattice, thus resulting in the reduction of crystallite size or enhancement of peak broadening. Crystallite size and peak shift $\delta\theta$ as a dependence of dopant concentration are plotted in Fig. 2a.

The lattice parameters 'a' and 'c' of a compound as a function of dopant concentration are given by the Vegard's law [33]. According to this law, the lattice parameter of the material compound with two different phases will be a linear function of unit cell composition. The ZnO lattice parameters 'a' and 'c' initially increase with lithium doping for $x \leq 3$ at.% and then decrease. Such a rapid expansion and compression of the lattice can be understood qualitatively by considering the sizes of the ions and their local coordination. Substitution of 0.74 Å sized Zn^{2+} ions with 0.60 Å sized Li^{1+} ions is expected to compress the interatomic spacing significantly, justifying the compression of the lattice. The decline in the lattice parameters for $x \geq 3$ at.% is in accordance with the Vegard's law. The variation in the lattice parameters 'a' and 'c' as a function of dopant concentration is depicted in Fig. 2b.

3.2 W–H plot and strain estimation

A mathematical expression relating the crystallite size and strain-induced broadening is proposed by Williamson and Hall. According to the expression, the peak width as a function of diffraction angle 2θ is considered for analyzing X-ray peak broadening [34, 35]. The relation is defined as $\beta_{\mathrm{hkl}} \cos\theta = (\frac{C\lambda}{R}) + (2\varepsilon \sin\theta)$ where β_{hkl} is the instrumental corrected FWHM in radians, R is the grain size in nm, λ is the X-ray wavelength in Å, C is a shape factor taken as 0.9 and ε is the strain induced on the particle. A plot shown in Fig. 2c is drawn with $\sin\theta/\lambda$ along x-axis and $\beta\cos\theta/\lambda$ along y-axis for high intense peak and, thus, the crystallite size and strain of $Zn_{1-x}Li_xO$ can be obtained from the inverse of the intercept at the y-axis and slope, respectively. The average crystallite size and strain estimated from the Scherrer relation and W–H plot are compared and tabulated in Table 1. From the table one can reveal that the average

Table 1 Geometric parameters of pure and lithium-doped ZnO particles

Samples	Scherrer method	W–H plot		Lattice parameters		Volume
	Crystallite size R (nm)	Crystallite size R (nm)	Strain ε (no unit)	'a' (Å)	'c' (Å)	(Å^3)
Li0	42	114	0.00270	3.2461	5.1968	47.423
Li1	91	109	0.00122	3.2454	5.1968	47.402
Li3	62	78	0.00128	3.2470	5.2022	47.470
Li6	55	77	0.00147	3.2460	5.1995	47.473
Li9	46	74	0.00210	3.2424	5.1896	47.251
Li15	39	73	0.00222	3.2404	5.1858	47.154

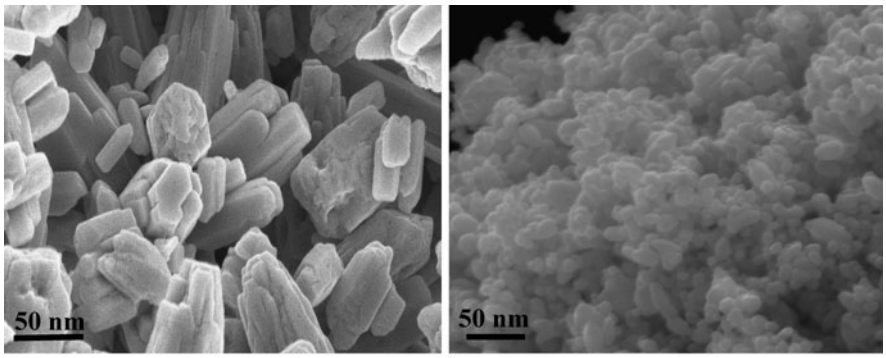

Fig. 3 (**a**–**b**) SEM micrographs of hydrothermally grown undoped (Li0) and doped ZnO (Li6)

crystallite size estimations from Scherrer relation and W–H plot are dissimilar. The vast difference in crystallite size calculation is mainly attributed to the inclusion of strain in the as-synthesized sample materials and their estimated strain values are reasonable. As more number of planes with varying intensity are present, it indicates the formation of polycrystalline grains with different orientations in Li:ZnO nanoparticles. Due to the crystallite size and inclusion of strain associated with the anisotropic nature of hexagonal crystal, there is a non-linear behavior in W–H plot. Thus, W–H plot serves as an additional tool to evaluate and deconvolute crystallite size and strain-induced broadening.

3.3 Morphology and structural analysis

Particle size distribution and direct images of the undoped and doped ZnO particles are observed from FESEM and TEM micrographs. Figures 3a and 3b are the high magnified (30.0 k magnification) SEM micrographs of undoped and 6 at.% Li-doped ZnO. It can be observed that the morphology and grain size are different with respect to doping. The image of pure ZnO sample in Fig. 3a indicates the formation of nanobundles where four to six short rods of varying size are bundled together. In the case of 6 at.% lithium-doped ZnO, particles are spherical in nature with high degree of agglomeration and aggregation. As the particles are aggregated, the diameter is not measured accurately. However, the TEM provides the actual size of the particles.

The TEM images of the undoped and lithium-doped ZnO nanoparticles are shown in Fig. 4. From the result of TEM images displayed in Fig. 4a it can be concluded that the morphology of pure ZnO is rod-shaped with non-uniform size and distribution. The individual nanorod has a length of about 375–500 nm and diameter of about 175 nm, producing an average aspect ratio of ∼2.5. The rods are long with blunt end resembling a hexagonal surface. This clearly demonstrates that the individual ZnO nanoparticles are self-assembled in the presence of long chain PEG molecule and oriented along a specific direction resulting in the formation of rod-shaped ZnO. In contrast, when the ZnO nanoparticles are doped with lithium atoms there is a morphology evolution from rod-shaped to particle nature. The incorporation of lithium inhibits the rate of particle growth but promotes the rate of nucleation, thus producing large number of particles in the given hydrothermal reaction period. This mechanism ultimately results in particle with reduced size close to 70–80 nm. The size measurement, estimated from TEM, well agrees with the crystallite size calculated using W–H method. The electron diffraction patterns of Li0 and Li6 are depicted as an inset in Figs. 4a and 4b, respectively. The measure of crystallinity and orientation of the particle growth are clearly predicted from the SAED pattern. The inset of Fig. 4a shows that the growth of ZnO nanorods is oriented along the c-axis plane (002) and the high intense regular dot pattern reveals the single crystalline nature of ZnO. In Fig. 4b the diffraction pattern is scattered and less in-

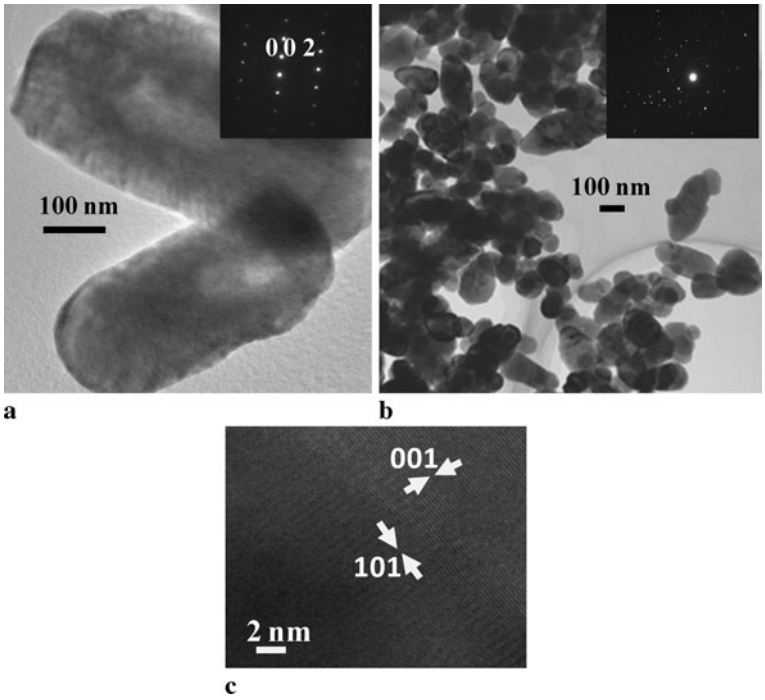

Fig. 4 (**a**–**b**) TEM images of undoped and Li6 nanoparticles; *the inset* shows their corresponding electron diffraction pattern. (**c**) HRTEM image of Li6

tense, revealing polycrystalline nature in lithium-doped ZnO nanoparticle with reduced crystallite size. Figure 4c is a lattice resolved high-resolution TEM (HRTEM) image of Li6 nanoparticles and their lattice orientations are labeled. The distance between two successive planes or the lattice spacing d measured from the fringe pattern is 2.47 and 2.58 nm, corresponding to (101) and (001) plane of hexagonal ZnO, confirming the crystalline nature and phase purity.

3.4 Band gap widening

Incorporation of lithium into the lattice of ZnO results in distinct difference in the optical absorbance spectrum. The UV absorption spectra of pure and doped ZnO as a function of wavelength are shown in Fig. 5a and the inset shows the method adopted to mark the onset of absorption for Li6. It is shown experimentally that an increase in hole concentration, the onset of absorption and the spectrum maximum are shifted towards the lower wavelength region. There is a significant change in the amount of absorbance due to the introduction of lithium atom into ZnO lattice. In lithium-doped ZnO nanoparticles, the UV-vis spectroscopy is blue-shifted by 10 nm (406–396 nm), due to widening of the band gap (see Fig. 5b). For the direct transition, the optical band gap energy of lithium-doped ZnO nanoparticles is determined using the Tauc plot relation $\alpha h\nu = C(h\nu - E_g)^{1/2}$ where $h\nu$ is the photon energy in eV, E_g is the optical band gap in eV and C is the constant [36]. The typical plot of $(\alpha h\nu)^2$ against the photon energy $h\nu$ for the ZnO nanoparticles, with and without the inclusion of lithium dopant, is shown in Fig. 6a. The direct band gap is determined by extrapolating and intersecting the linear portion of $(\alpha h\nu)^2$ to the energy axis $h\nu = 0$ (see the inset of Fig. 6a). From the graph, the calculated band gap energy of undoped and doped ZnO comes out to be 3.21, 3.156, 3.189, 3.193, 3.197 and 3.202 eV for Li0, Li1, Li3, Li6, Li9 and Li15, respectively. Figure 6b clearly pictures that the lithium doping widens the band gap energy by an order of 46 meV.

The observed blue shift in the absorption wavelength is the reflection of the band gap widening, owing to size confinement effect. However, the QSE is highly pronounced only when the crystallite size of ZnO nanocrystalline semiconductor is comparable to its Bohr exciton radius. But, the crystallite sizes of lithium-doped ZnO calculated from XRD and TEM are far beyond the quantum confinement regime. As a result, the shift in absorption edge and widening of the band gap can be explained on the basis of Burstein–Moss shift and it is well pronounced in heavily doped semiconductor [37]. Since these are degenerate p-type semiconductors, the Fermi level lies within the valence band, and their position depends on the concentration of the holes. Thus, the optical band gap values calculated from UV absorbance are related to the excitation of the electrons from the Fermi level in the valance band to the conduction band, whereas the actual band gap of the material is related to the excitation of the electrons from the top of the valence band to the bottom of the conduction band. The increase of the optical band gap energy with increase in dopant concentration is attributed to the Burstein–Moss effect. In lithium-doped ZnO nanoparticles, when more and more free carrier holes are added, the topmost electronic states in valence band become vacant

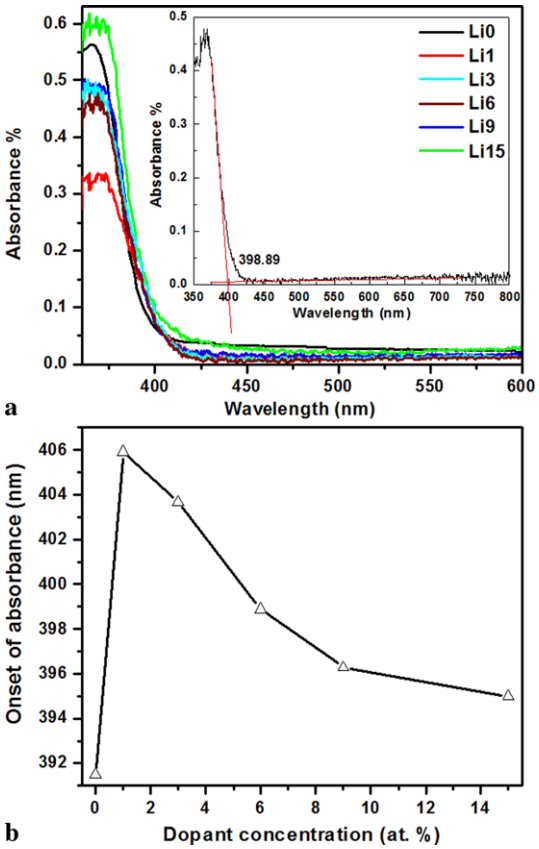

Fig. 5 (**a**) UV absorption spectra of $Zn_{1-x}Li_xO$ ($x = 0$, 1, 3, 6, 9, and 15 at.%); *the inset* shows the point of intersection measured for Li6. (**b**) Change in onset of absorption as a function of lithium percentage

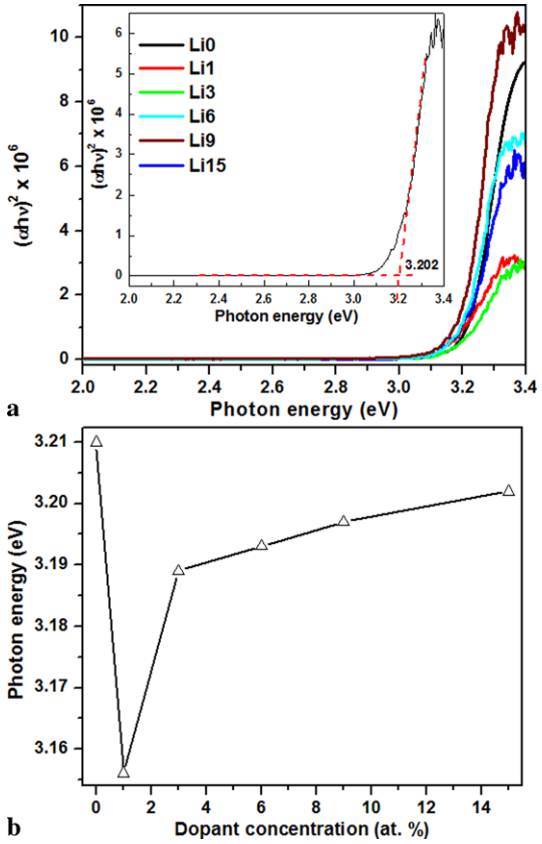

Fig. 6 (**a**) Tauc plot relation; *the inset* shows the band gap estimation for Li6. (**b**) Variation in the optical band gap energy as a function of dopant concentration

and, hence, shift the absorption edge towards higher photon energy. The shift in Fermi energy level prohibits the intermediate transition or interband transition through Pauli's exclusion principle. Additionally, the PL measurements are carried out to confirm the absence of impurity band formation, band to shallow acceptor transition and correlate the observed band gap widening.

3.5 Luminescence spectrum

The onset of emission, peak position, presence of intermediate transition or impurity band transition and the efficiency of luminescence spectrum are well described in PL spectra. A plot of normalized PL intensity against the photon energy for lithium-doped ZnO under the excitation of 230 nm wavelength is shown in Fig. 7a. The room temperature PL spectra of hydrothermally synthesized lithium-doped ZnO nanoparticles exhibit strong UV emission near the band edge and the peaks shift to higher photon energy as the lithium concentration increases, indicating a broadening of the band gap. The PL spectra of Li0 (see Fig. 7a) show two emission peaks, centered at 3.13 and 2.70 eV, that can be assigned to the recombination of excitons and blue emission due to oxygen vacancies and interstitial defects. Figure 7b shows that the NBE emission in the PL spectra of lithium-doped ZnO nanoparticles are highly blue-shifted from ∼2.8 to ∼3.15 eV. The blue shift in the NBE emission cannot be caused by the quantum confinement effect as explained earlier under the head band gap widening (see Sect. 3.4). The hydrothermal chemical precipitation is employed to obtain defect-free lithium-doped ZnO, as the blue band emissions due to oxygen vacancies are completely suppressed in their emission spectrum. The experimental data obtained from absorption and PL measurement well agrees and supports the validity of Burstein–Moss shifts. Figure 7b compares the blue shift in optical band gap and NBE emission of lithium-doped ZnO.

Figure 7c easily portraits the overall mechanism involved in band gap widening of lithium-doped ZnO. In *p*-type semiconductor the Fermi energy level lies close to the valence band. As the free carrier concentration (hole) adds up, the position of Fermi level gets disturbed and shifted within the valence band. Due to the inclusion of holes or a vacant energy state, the electrons in the valence band make a transition to occupy the available states. This transition and the periodic addition of holes make the Fermi level to shift furt-

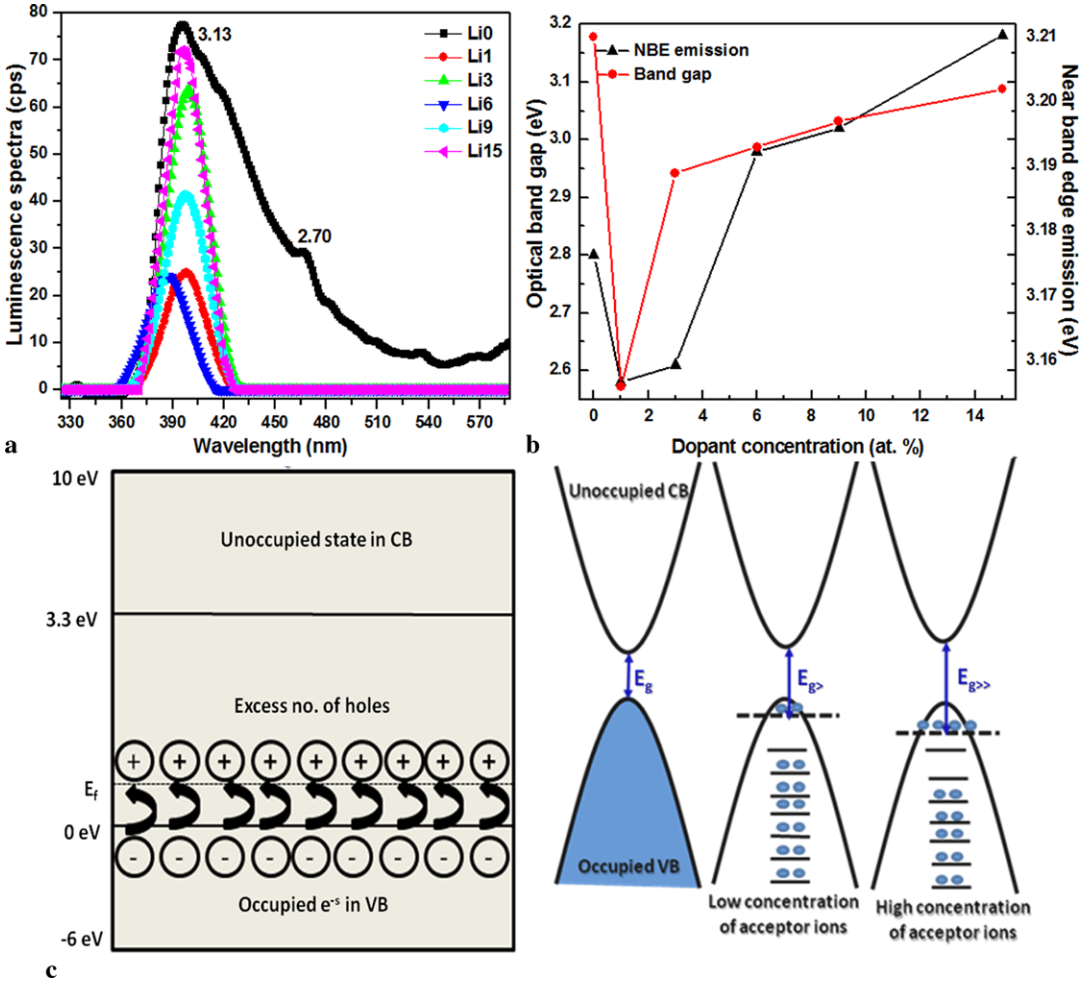

Fig. 7 (**a**) Room temperature luminescence spectra of $Zn_{1-x}Li_xO$ ($x = 0$, 1, 3, 6, 9, and 15 at.%) excited under the wavelength of 230 nm. (**b**) Variation in the optical band gap and near-band-edge emission with increase in dopant densities. (**c**) Schematic illustration of the Burstein–Moss shift in lithium-doped ZnO

Table 2 Optical measurements of $Zn_{1-x}Li_xO$ ($x = 0$, 1, 3, 6, 9, and 15 at.%) particles

Samples	UV absorption spectra		Luminescence spectra	
	Onset of absorption (nm)	Optical band gap energy (eV)	NBE emission (eV)	Blue emission (eV)
Li0	392	3.210	3.13	2.70
Li1	406	3.156	3.11	–
Li3	404	3.189	3.11	–
Li6	399	3.193	3.13	–
Li9	396	3.197	3.13	–
Li15	395	3.202	3.14	–

her below the valence band and thus widen the band gap. Table 2 summarizes the optical measurements extracted from the UV absorbance spectrum, as well as from the PL spectra, of pure and lithium-doped ZnO nanoparticles.

3.6 FT-IR study

The formation of lithium-doped ZnO powders and metal–oxide interaction are well identified from FT-IR study. Figure 8 shows the FT-IR transmission spectra of pure and

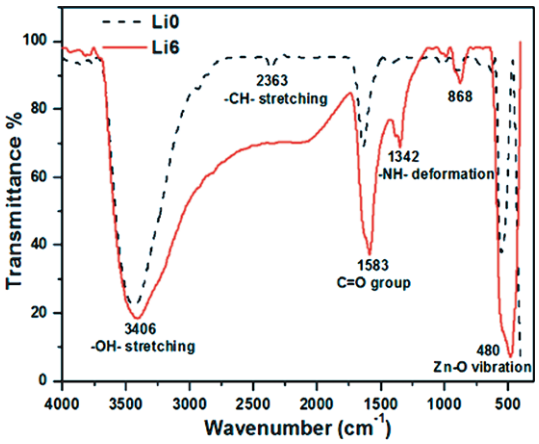

Fig. 8 FT-IR transmission spectra of pure ZnO and Li6 nanoparticles

6 at.% lithium-doped ZnO. In the figure, sharp distinct vibrational bands at 600 and 400 cm^{-1} are observed and are attributed to ZnO stretching vibrations [38]. The fundamental characteristic vibrational band at 506 cm^{-1} shift towards lower wavenumber at 480 cm^{-1} and is broadened for 6 at.% lithium-doped ZnO nanoparticles. This broadening signifies that the lithium-doped ZnO are of reduced particle size compared to undoped ZnO. The –CH– stretching band belonging to the PEG block appears between 2300 and 2830 cm^{-1} [39]. The transmittance at 1342 cm^{-1} is assigned to the deformation of NH. The broad absorption in the frequency band 3000–3750 cm^{-1} and a sharp absorption at 1600 cm^{-1} in the higher frequency range are assigned to the O–H stretching from residual alcohols, water and Zn–OH bonds. The absorption at 1600 cm^{-1} is associated with the deformation vibration of H–O–H bonds of the physisorbed water.

4 Conclusions

Morphology evolution of doped ZnO is obtained through low-temperature hydrothermal method. HRTEM studies showed that the Li6 nanoparticles are oriented along (101) and (001) plane. Room temperature UV absorption spectrum revealed that the introduction of lithium ions in ZnO can tune the band gap of the nanocrystals in the range of 3.15–3.20 eV. The luminescence spectrum of lithium-doped ZnO is defect-free and exhibits only band edge emission at room temperature. Results indicate that the spontaneous contraction of the surface chemical bonds and the increase in surface-to-volume ratio with reduced particle size are responsible for the change in band structure of lithium-doped ZnO nanoparticles. The Burstein–Moss effect served as a supportive tool in explaining the observed band gap widening associated with lithium-doped ZnO. In conclusion, the optical properties of ZnO vary conspicuously with obvious change in the dopant concentration.

Acknowledgements The authors thank Dr. M. Chidambaram, Director, National Institute of Technology, Tiruchirappalli for his constant encouragement and support. We also thank Dr. Justin Josephus and Dr. M. Ashok, Assistant Professor, National Institute of Technology, Tiruchirappalli for acquiring the TEM micrographs and UV-vis absorption spectrum respectively. This research was financially supported by TEQIP and DST project (SR/FTP/ETA-31/07), Government of India.

References

1. J. Yu, X.O. Yu, Environ. Sci. Technol. **42**, 4902 (2008)
2. Z. Fan, J.G. Lu, Int. J. High Speed Electron. Syst. **16**, 883 (2006)
3. O. Lupan, G. Chai, L. Chow, Microelectron. Eng. **85**, 2220 (2008)
4. E. Galoppini, J. Rochford, H. Chen, G. Saraf, Y. Lu, A. Hagfeldt, G. Boschloo, J. Phys. Chem. Lett. B **110**, 16159 (2006)
5. B.S. Ong, C. Li, Y. Li, Y. Wu, R. Loutfy, J. Am. Chem. Soc. **129**, 2750 (2007)
6. R. Konenkamp, R. Word, C. Schlegel, Appl. Phys. Lett. **85**, 6004 (2004)
7. R.M. Nyffenegger, B. Craft, M. Shaaban, S. Gorer, G. Erley, R.M. Penner, Chem. Mater. **10**, 1120 (1998)
8. Z.L. Wang, J. Phys., Condens. Matter **16**, R829 (2004)
9. U. Ozgur, Y.I. Alivov, C. Liu, A. Teke, M.A. Reshchikov, S. Doğan, V. Avrutin, S.J. Cho, H. Morkoc, J. Appl. Phys. **98**, 041301 (2005)
10. L. Schmidt-Mende, J.L. MacManus-Driscoll, Mater. Today **10**, 40 (2007)
11. S. Baruah, S. Dutta, J. Sci. Technol. Adv. Mater. **10**, 013001 (2009)
12. J.C. Johnson, H. Yan, P. Yang, R.J. Saykally, J. Phys. Chem. B **107**, 8816 (2003)
13. L.S. Hsu, C.S. Yeh, C.C. Kuo, B.R. Huang, S. Dhar, J. Optoelectron. Adv. Mater. **7**, 3039 (2005)
14. G.D. Yuan, W.J. Zhang, J.S. Jie, X. Fan, J.A. Zapein, Y.H. Leung, L.B. Luo, P.F. Wang, C.S. Lee, S.T. Lee, Nano Lett. **8**, 2591 (2008)
15. Y. Miao, Z. Ye, W. Xu, F. Chen, X. Zhou, B. Zhao, L. Zhu, J.G. Lu, J. Appl. Surf. Sci. **252**, 7953 (2006)
16. T. Aoki, Y. Shimizu, A. Miyake, A. Nakamura, Y. Nakanishi, Y. Hatanaka, Phys. Status Solidi B **229**, 911 (2002)
17. H.J. Xiang, J. Yang, J.G. Hou, Q. Zhu, Appl. Phys. Lett. **89**, 223111 (2006)
18. K. Ellmer, R. Mientus, Thin Solid Films **516**, 4620 (2008)
19. B. Yi, C.C. Lim, G.Z. Xing, H.M. Fan, L.H. Van, S.L. Huang, K.S. Yang, X.L. Huang, X.B. Qin, B.Y. Wang, T. Wu, L. Wang, H.T. Zhang, X.Y. Gao, T. Liu, A.T.S. Wee, Y.P. Feng, J. Ding, Phys. Rev. Lett. **104**, 137201 (2010)
20. W. Xie, Z. Yang, H. Chun, Ind. Eng. Chem. Res. **46**, 7942 (2007)
21. A.H. Salama, F.F. Hammad, J. Mater. Sci. Technol. **25**, 314 (2009)
22. Q. Zhang, C.S. Dandeneau, S. Candelaria, D. Liu, B.B. Garcia, X. Zhou, Y.H. Jeong, G. Cao, Chem. Mater. **21**, 4087 (2010)
23. R.N. Bhargava, D. Haranath, A. Mehta, J. Korean Phys. Soc. **53**, 2847 (2008)
24. M. Wu, L. Yao, W. Cai, G. Jiang, X. Li, Z. Yao, J. Mater. Sci. Technol. **20**, 11 (2004)
25. J. Wang, X.P. An, Q. Li, R.F. Egerton, Appl. Phys. Lett. **86**, 201911 (2005)
26. B.R. Bennett, R.A. Soref, A.D. Alamo, J. Quantum Electron. **26**, 113 (1990)
27. Y. Gu, I.L. Kuskovsky, M. Yin, S. O'Brien, G.F. Neumark, Appl. Phys. Lett. **85**, 3833 (2004)
28. A. Walsh, J.L.F. Da Silva, S.H. Wei, Phys. Rev. B **78**, 075211 (2008)

29. B. Saha, R. Thapa, K.K. Chattopadhyay, Solid State Commun. **145**, 33 (2008)
30. H.C. Hsu, C.Y. Wu, H.M. Cheng, W.F. Hsieh, Appl. Phys. Lett. **89**, 013101 (2006)
31. T. Makino, Y. Segawa, S. Yoshida, A. Tsukazaki, A. Ohtomo, M. Kawasaki, Appl. Phys. Lett. **85**, 759 (2004)
32. N.R. Yogamalar, R. Srinivasan, A. Chandra Bose, Opt. Mater. **31**, 1570 (2009)
33. H.L. Shi, Y. Duan, Eur. Phys. J. B **66**, 439 (2008)
34. V. Biju, S. Neena, V. Vrinda, S.L. Salini, J. Mater. Sci. **43**, 1175 (2008)
35. N.R. Yogamalar, R. Srinivasan, A. Vinu, K. Ariga, A. Chandra Bose, Solid State Commun. **149**, 1919 (2009)
36. L. Xiao-bo, S. Hong-Lie, Z. Hui, L. Bin-bin, Trans. Nonferr. Met. Soc. China **17**, s814 (2007)
37. P.D.C. King, T.D. Veal, F. Fuchs, C.Y. Wang, D.J. Payne, A. Bourlange, H. Zhang, G.R. Bell, V. Cimalla, O. Ambacher, R.G. Egdell, F. Bechstedt, C.F. McConville, Phys. Rev. B **79**, 205211 (2009)
38. N.R. Yogamalar, S. Anitha, R. Srinivasan, A. Vinu, K. Ariga, A. Chandra Bose, J. Nanosci. Nanotechnol. **9**, 5966 (2009)
39. A. Thangaraja, V. Savitha, K. Jegatheesan, Int. J. Nanotechnol. Appl. **4**, 31 (2010)